Capture and chaotic scattering of a charged particle by a magnetic monopole under a uniform electric field

Kou Misaki[1] and Naoto Nagaosa[1,2]
[1]*Department of Applied Physics, The University of Tokyo, Bunkyo, Tokyo 113-8656, Japan*
[2]*RIKEN Center for Emergent Matter Science (CEMS), Wako, Saitama 351-0198, Japan*

(Received 12 July 2018; published 27 November 2018)

Motivated by the realization of a magnetic monopole of Berry curvature by the energy crossing point, we study theoretically the effect of a magnetic monopole under a uniform electric field in semiclassical wave-packet dynamics, which is relevant to many physical situations such as relaxation through the diabolic point. We found that the competition between backward scattering by a monopole magnetic field and acceleration by an electric field leads to a bound state, i.e., capture of a particle near the monopole. Furthermore, the nonlinearity induced by the magnetic monopole leads to chaotic behavior in transient dynamics, i.e., transient chaos. We computed the characteristic quantities of the strange saddle, which gives rise to transient chaos, and we verified that the abrupt bifurcation occurs as we tune the system parameter toward the parameter region in which the system is solvable.

DOI: 10.1103/PhysRevE.98.052225

I. INTRODUCTION

Ever since Dirac pointed out the possible existence of a magnetic monopole by considering the 2π ambiguity of the phase of an electron wave function [1], it has attracted broad theoretical interest and appeared in many areas of physics [2–4]. In particular, the magnetic monopole of Berry curvature [5] or a synthetic gauge field [6,7] appears both in real [8–10] and momentum [11–14] space, and it has a drastic effect on the transport property as it modifies the semiclassical equation of motion for the wave packet of particles [15–18].

Actually, the history of the magnetic monopole [19–23] dates back to the late 1800s, when Darboux and Poincaré studied the problem of electron scattering by a magnetic monopole [24,25]. This problem is known to be exactly solvable, and it exhibits some unusual properties [22] (see Appendixes A and B for a review of the exact solution). In this paper we will show that, upon introducing a uniform electric field, the peculiar nature of this scattering problem leads to chaotic dynamics, i.e., chaotic scattering [26–31]. We note that although the formulation itself is purely classical, our model can be viewed as a semiclassical approximation, i.e., considering the first order in $\hbar$ expansion of wave-packet dynamics in a multilevel system [18]. Here Berry curvature, which appears in the form of a magnetic field, is a quantum correction to purely classical dynamics, and it is known that the energy crossing point acts as a magnetic monopole [5,32], so our model can be viewed as a semiclassical approximation to relaxation dynamics in a two-level system, where the wave packet passes near the degenerate point.

II. MODEL

We study numerically the equation describing the dynamics of a particle under the influence of a monopole magnetic field and a uniform electric field:

$$m\frac{d^2\vec{r}}{dt^2} = f\vec{e}_z + q_m q_e \frac{d\vec{r}}{dt}\times\frac{\vec{r}}{r^3}, \tag{1}$$

where m is the mass of the particle, f is the uniform force along the z direction, and q_m and q_e are the magnetic charge of the monopole sitting at the origin and the electric charge of the particle, respectively. This equation has two conserved quantities, i.e., the energy and the angular momentum along the z direction:

$$E = \frac{m}{2}(\dot{\vec{r}})^2 - fz, \quad J_z = m(x\dot{y} - y\dot{x}) - q_m q_e \frac{z}{r}, \tag{2}$$

where the second term of J_z comes from the angular momentum of the electromagnetic field. We can utilize J_z conservation to reduce one degree of freedom, as follows. The Lagrangian for our model can be written as

$$L = \frac{m}{2}(\dot{\rho}^2 + \dot{z}^2 + \rho^2\dot{\phi}^2) - q_m q_e \frac{z}{\sqrt{\rho^2+z^2}}\dot{\phi} + fz, \tag{3}$$

where (ρ, ϕ, z) represent the cylindrical coordinates, and the vector potential $A_\phi = -q_m q_e z/\sqrt{\rho^2+z^2}$ comes from the magnetic monopole at the origin. Since ϕ is the cyclic coordinate of the system, the conjugate momentum J_z, Eq. (2), is conserved. Then, we can construct the Routhian [33]:

$$\begin{aligned} R &= L - J_z\dot{\phi}|_{\dot{\phi}=(J_z+q_m q_e \frac{z}{\sqrt{\rho^2+z^2}})/(m\rho^2)} \\ &= \frac{m}{2}(\dot{\rho}^2 + \dot{z}^2) \\ &\quad - \frac{1}{2m\rho^2}\left(J_z + q_m q_e \frac{z}{\sqrt{z^2+\rho^2}}\right)^2 + fz. \end{aligned} \tag{4}$$

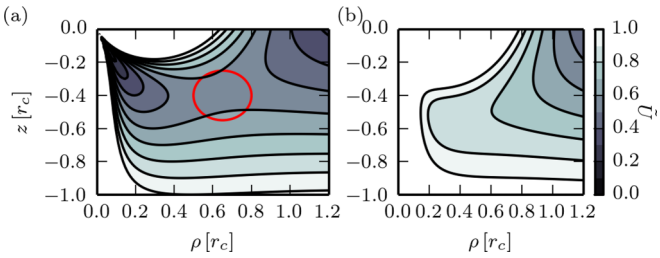

FIG. 1. The distribution of $U_{\rm eff}$ in the (ρ, z) plane for (a) $J_z/(q_m q_e) = 0.9$ and (b) $J_z/(q_m q_e) = \sqrt{32/27} + 0.01$. The color represents the potential height $\tilde{U} := U_{\rm eff}/(f r_c)$, where $r_c := |q_m q_e|^{2/3}/(mf)^{1/3}$, as is shown in the right of (b). We can see the potential saddle that we highlighted with a red circle for (a), while the saddle disappears for (b).

The dynamics is now described by two degrees of freedom (ρ, z), and the potential energy is modified as follows:

$$m\frac{d^2 z}{dt^2} = -\frac{\partial U_{\rm eff}}{\partial z}, \qquad m\frac{d^2 \rho}{dt^2} = -\frac{\partial U_{\rm eff}}{\partial \rho}, \qquad U_{\rm eff} := -fz + \frac{\left(J_z + \dfrac{q_m q_e z}{\sqrt{z^2+\rho^2}}\right)^2}{2m\rho^2}. \tag{5}$$

The form of the potential depends on the value of J_z, which is determined from the initial conditions according to Eq. (2). As we can see from Fig. 1(a), there exists a potential saddle for a particular parameter range of J_z. If we consider the dynamics of the particle starting from the initial position inside the potential pocket bounded by the saddle and the potential walls, the particle bounces back and forth inside the pocket and eventually goes over the saddle. Therefore, the saddle and the potential pocket that it bounds are crucial ingredients for this scattering problem; and we discuss the conditions for its existence in the next section.

Since the diverging magnetic field leads to an infinite cyclotron frequency, it invalidates the numerical calculation for the trajectory passing near the origin. To avoid this difficulty, we introduce a smeared magnetic charge:

$$p(\vec{r}) = \frac{1}{\xi^3\sqrt{\pi^3}} \int d\vec{R}\, e^{-\frac{|\vec{r}-\vec{R}|^2}{\xi^2}} q_m \delta(\vec{R}) = \frac{q_m e^{-\frac{r^2}{\xi^2}}}{\xi^3\sqrt{\pi^3}}. \tag{6}$$

The magnetic field produced by this magnetic charge is the same as the monopole for $r \gg \xi$, and it converges to 0 as $r \to 0$.

III. RESULT

We performed numerical calculation of Eq. (1) with the Runge-Kutta method and the implicit Tajima method [34]. We can regard the dynamics described by Eq. (1) as a problem of charged particle scattering by a magnetic monopole. There are two important physical observables: $t_{\rm pass}$, which is the time it takes for the particle to get out of the scattering region, which we define as $r \leqslant 2r_c$ [$r_c := |q_m q_e|^{2/3}/(mf)^{1/3}$], and $r_{\rm min} := \min_t\{r(t)\}$, which determines whether our approximation of the point magnetic charge by the smeared one is good or not. We set the initial velocity to zero, we vary $z(0) = z_0$ and $x(0) = x_0$ to adjust the incident velocity and the impact parameter, respectively, and we set $q_m q_e < 0$. We show the result of the numerical calculation in Fig. 2. For the small x_0 (small J_z) and small $|z_0|$ (small energy) regions, we observed that $t_{\rm pass}$ becomes larger than the numerically accessible time region. This fact can be understood from the geometry of the effective potential, Eq. (5): For this region, the particle cannot escape from the scattering region since the height of the potential saddle is higher than the initial energy; the condition for the existence of this region can be obtained as shown below.

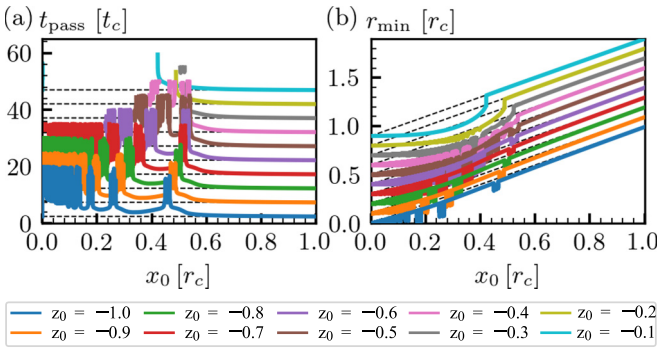

FIG. 2. The time when the particle got out of the scattering region $r \leqslant 2r_c$ ($t_{\rm pass}$) and the minimum value of $r(t)$ [$r_{\rm min} := \min_t(r(t))$] for the initial position $(x_0, 0, z_0)$. Here $r_c := |q_m q_e|^{2/3}/(mf)^{1/3}$ and $t_c := (m|q_m q_e|)^{1/3}/f^{2/3}$. Numerical calculation was done with an implicit Tajima method. The black dashed line represents the values without the monopole magnetic field. Note that each plot is shown with an offset. The values of the offset are given by the values of the dashed line at $x_0 = 0$. For small x_0 and z_0, $t_{\rm pass}$ is larger than $t/t_c = 20$, and the plot of $t_{\rm pass}$ at these values is not shown.

If we vary the two parameters (x_0, z_0), $J_z(x_0, z_0)$ and $E_0(z_0)$ change, and for small E_0 and large J_z the region with $E \leqslant E_0$ is separated and confined to the finite region, as we can see from Fig. 3(c), thereby leading to the infinite $t_{\rm pass}$. For smaller J_z, the two regions are connected by a saddle with energy height $E_{\rm saddle} < E_0$, leading to finite $t_{\rm pass}$. To obtain the analytical expression of the boundary between these two cases in the (J_z, E_0) plane, we observe that

$$U_{\rm eff} = E_0 \Leftrightarrow 2\sin v \cos^2 v R^3 + 2\epsilon_0 \cos^2 v R^2 - (\sin v + \tilde{J}_z)^2 = 0, \tag{7}$$

where $Z := r_c z$, $P := r_c \rho$, $R := r_c r$, $Z = R\sin v$, $P = R\cos v$, $r_c = |q_m q_e|^{2/3}/(mf)^{1/3}$, $\tilde{J}_z := J_z/(q_m q_e)$, and $\epsilon_0 := E_0/(f r_c)$. The necessary condition for the merger of two separate regions is that the discriminant for this third-order polynomial for R is zero:

$$\sin^4 v + 2\tilde{J}_z \sin^3 v + \left(\tilde{J}_z^2 + \alpha\right)\sin^2 v - \alpha = 0, \tag{8}$$

where $\alpha := 8\epsilon_0^3/27$. Furthermore, we impose the condition that the discriminant for this fourth-order polynomial for $\sin v$ is zero:

$$\alpha^2\left[\alpha^3 + \left(3\tilde{J}_z^2 + 8\right)\alpha^2 + \left(3\tilde{J}_z^4 - 20\tilde{J}_z^2 + 16\right)\alpha + \tilde{J}_z^4\left(\tilde{J}_z^2 - 1\right)\right] = 0. \tag{9}$$

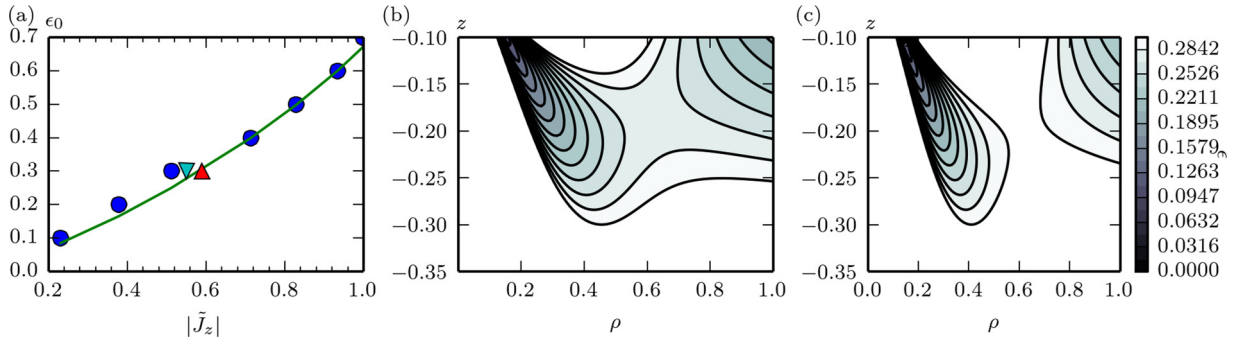

FIG. 3. (a) The boundary separating the trapping orbit and the escaping orbit. The dots are the results of numerical calculation, and the line represents the analytic expression Eq. (10). (b), (c) The contour plot for the energy range $0 < \epsilon < \epsilon_0 = 0.3$ and $\tilde{J}_z = 0.55$ and 0.59 for (b) and (c), respectively. The parameter values for (b) and (c) are shown by the blue down-triangle and the red up-triangle in (a), respectively.

Solving this equation for α, we obtain five solutions. Choosing the relevant solution, we obtain

$$\epsilon_0 = \left(-\frac{9}{8}(8 + 3\tilde{J}_z) + \frac{9}{2}\frac{4 + 27\tilde{J}_z^2}{G} + \frac{9}{8}G \right)^{\frac{1}{3}}, \tag{10}$$

where G is given as

$$\left(64 - 1080\tilde{J}_z^2 - \frac{729\tilde{J}_z^4}{2} + \frac{3\sqrt{3}}{2}\sqrt{\tilde{J}_z^2\left(-32 + 27\tilde{J}_z^2\right)^3} \right)^{\frac{1}{3}}. \tag{11}$$

The plot of this curve is shown by the solid line in Fig. 3(a). In addition, we obtain the value of J_z where the saddle point of the potential energy vanishes: Above $\tilde{J}_z^2 = 32/27$, the right-hand side of Eq. (10) becomes complex, meaning that there is no saddle in the potential energy. Since the chaotic scattering is caused by the pocket of energy minimum bounded by the saddle, we expect no chaotic scattering above this J_z, so we concentrate on the dynamics for this range of J_z.

In addition, we can see the complicated peak structure in the region with a small impact parameter, and as is shown in Fig. 4, each peak has a fractal structure, and the scattering angle Θ, which is the relative angle between the initial and the final velocity, varies very wildly near this peak structure. We show the dynamics at each hierarchy of the fractal in Fig. 5. We checked the convergence of the peak structure and the small error of conserved quantities, so this peak structure is not an artifact of the finite precision of the numerical calculation. Actually, this fractal structure of $t_{\rm pass}$ is a characteristic feature of the chaotic scattering [30,31], which is a representative example of the transient chaos of Hamiltonian systems [35,36].

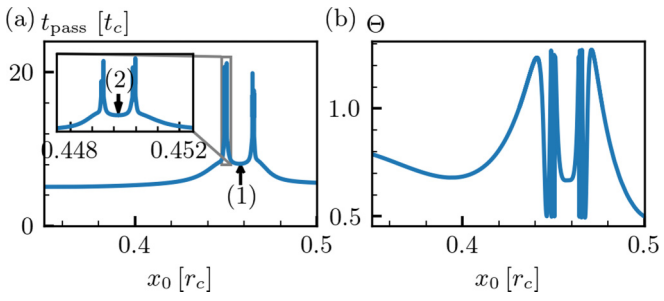

FIG. 4. (a) The peak structure of $t_{\rm pass}$ around $x_0/r_c \cong 0.45$ at $z_0/r_c = -1$. The inset shows the detailed peak structure of the left peak, and we can clearly see the self-similarity of the peak. We showed (1) and (2), which is the parameter point we take for the dynamics shown in Fig. 5. We define the parameter points (n) for all n larger than 2 for finer structures in the same way. (b) The rapid variation of $\Theta := \cos^{-1}[v_z(t_{\rm pass})/\sqrt{\vec{v}(t_{\rm pass}) \cdot \vec{v}(t_{\rm pass})}]$ near the fractal peak, which is the characteristic feature of chaotic scattering [30,31].

To understand why chaotic scattering occurs and why there are multiple peaks for each z_0, it is convenient to go back to the $f = 0$ limit of Eq. (1). As we mentioned in the Introduction, this model is solved exactly. Among some peculiar characteristics, one notable feature is the impact parameter (x_0) dependence of the scattering angle: There are multiple backscattering points (so-called glory scattering) located at $q_e q_m/(mvx_0) = \sqrt{4n^2 - 1}$ $(n = 1, 2, \dots)$, where v represents the initial velocity [37,38]. This is in sharp contrast to the scattering angle in the Rutherford scattering, which has a monotonic impact parameter dependence. If we regard each backscattering point as a potential hill, the situation is formally similar to the scattering problem by multiple scatterers, which is known to exhibit chaotic behavior at a transient time scale [30,31]. Moreover, for fixed z_0 there are infinitely many x_0 where the particle is backscattered, and this leads to infinitely many well-separated peak structures (see Appendix C).

The chaotic scattering can be understood as a consequence of the fractional dimension of the saddle induced

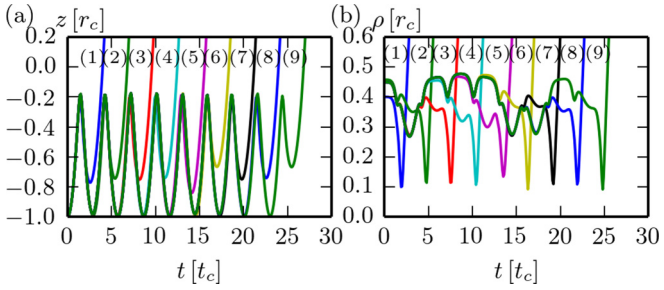

FIG. 5. (a) $z(t)$ and (b) $\rho(t)$. The value of x_0 at (n) is defined in Fig. 4. We can see the correspondence between the number of the oscillation and the number of the hierarchy.

by horseshoe mapping [39]. The fact that the saddle has a fractal dimension has a drastic consequence on the physical quantities: The dimension of generic crossing of the stable manifold of the saddle and the one-parameter family of initial conditions in phase space becomes fractional. As a result, at each intersection the time it takes for the particle to get out of the scattering region ($t_{\rm pass}$) is infinite, so $t_{\rm pass}$ has a peak on the set with a fractional dimension. The dimension of crossing can be calculated as follows [40]: Our model is a Hamiltonian system with two degrees of freedom [Eq. (5)]. Within each energy shell, the dimension of phase space is 3. Noting that Eq. (5) has time-reversal symmetry, the dimensions of the stable and the unstable manifold are the same. Since the dimension of the intersection of the two subsets S_1 and S_2 in the d-dimensional manifold ($d = 3$ in our case) is given by $D(S_1 \cap S_2) = D(S_1) + D(S_2) - d$, where $D(S)$ represents the dimension of S, and the saddle is given by the intersection of the stable and the unstable manifold, $D(S_{\rm st}) = [D(S_{\rm sad}) + 3]/2$, where $S_{\rm sad}$ and $S_{\rm st}$ represent the saddle and the stable manifold of the saddle. Therefore, the dimension of crossing, which we refer to as the fractal dimension, is given by $d_{\rm fra} = 1 + D(S_{\rm st}) - 3 = [D(S_{\rm sad}) - 1]/2$.

Concerning the dynamics on the saddle, the positivity of the Lyapunov exponent itself does not immediately imply chaotic behavior, which can be quantitatively understood from the following Kantz-Grassberger formula [31,36,41,42]: $\sum_{\lambda_i>0} \lambda_i = \kappa + h_{\rm KS}$, where λ_i's are the Lyapunov exponents of the invariant set, κ is the escape rate, i.e., $\kappa := \lim_{T\to\infty} -(1/T)\ln(N(T)/N(0))$ [$N(T)$ is the number of particles remaining in the scattering region at $t = T$], and $h_{\rm KS}$ is the Kolmogorov-Sinai entropy, of which a nonzero value implies chaos. This equation represents the fact that the instability of the invariant set (Lyapunov exponent) leads to two phenomena: the escape of the particle from the scattering region, and the growth of the information, which is a characteristic feature of chaos. As we can see, positive λ_i with $h_{\rm KS} = 0$ is possible because of the finite escape rate κ in contrast to the case with the attractor. For the numerical calculation, Young's formula [42,43] is useful: For a Hamiltonian system with two degrees of freedom, it is $h_{\rm KS} = \lambda(D_1 - 1)/2$, where D_1 is the information dimension in 3D phase space, and it is defined by

$$D_1 := \lim_{q\to 1} D_q := \lim_{q\to 1}\lim_{\delta\to 0} \frac{1}{q-1}\frac{\log\sum_i p_i^q}{\log\delta}, \qquad (12)$$

where δ is the linear size of the box we use to divide the phase space to define the measure p_i, and D_q is the Rényi dimension. Compared to the box-counting dimension of the invariant set (D_0), the information dimension reflects the property of the dynamics on the set through the invariant measure p_i.

As is explained above, the information of the saddle that characterizes the chaotic behavior can be understood from the following quantities: κ, λ_i, D_0, D_1, and $h_{\rm KS}$. In the following, we calculate the characteristic quantities of the fractal peak for $z_0 = -1$ near $x_0 = 0.45$ to confirm that what we found is transient chaos [31].

First, we calculate the uncertainty exponent [36]. [We defined $|t_{\rm pass}(x_0+\epsilon) - t_{\rm pass}(x_0)| > 0.5$ as the uncertain pair [44].] We obtained $d_{\rm fra} = 1 - d_{\rm unc} = 0.259 \pm 0.008$. We calculated this exponent for different values of the dimensionless force parameter $F = f\tilde{r}_c/E$, where $\tilde{r}_c = |q_m q_e|/\sqrt{mE}$, with the total energy E fixed. The $F = 1$ limit corresponds to the original model Eq. (1) with $\vec{r}(0) = (x_0, 0, -\tilde{r}_c)$ and $\vec{v}(0) = \vec{0}$, while $F = 0$ corresponds to $f = 0$ in Eq. (1) (i.e., the solvable limit [22]) with $\vec{r}(0) = (x_0, 0, -\tilde{r}_c)$ and $\vec{v}(0) = (0, 0, \sqrt{2E/m})$ [45]. We found that the abrupt bifurcation similar to the potential scattering problem [31] occurs around $F \sim 0.87$; see Fig. 6.

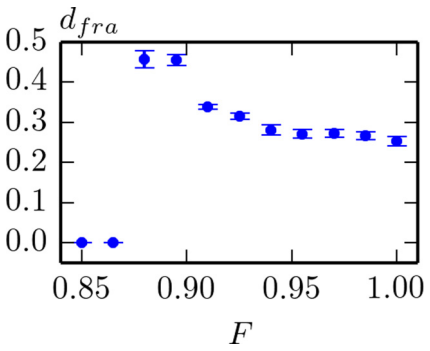

FIG. 6. The abrupt bifurcation observed by varying the force term toward zero. $F = f\tilde{r}_c/E$ is the dimensionless force parameter, where $\tilde{r}_c = |q_m q_e|/\sqrt{mE}$ and E is the total energy of the particle. $F = 1$ corresponds to the original parameter, and $F = 0$ corresponds to the solvable, zero force limit. We can see that the fractal dimension abruptly drops to zero around $F \sim 0.87$. The value of F used to calculate the quantities discussed in the main text corresponds to $F = 1$.

Secondly, we calculate the invariant measure of the strange saddle on the Poincaré section defined by $z = -0.5r_c$. We note that our system has two degrees of freedom with energy conservation; see Eq. (5). Accordingly, the dimension of the Poincaré section is $3 - 1 = 2$ (remember that the phase-space dimension is 3), and we take the coordinate as $(\rho, d\rho/dt)$, where $\rho = \sqrt{x^2 + y^2}$. The result is shown in Fig. 7. From this invariant measure, we can calculate

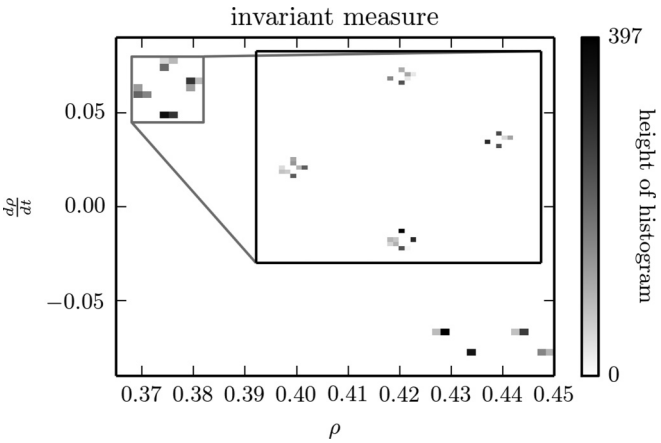

FIG. 7. The invariant measure of the strange saddle on the Poincaré section defined by $z = -0.5r_c$ and $v_z > 0$, obtained by the PIM-triple method [31,46]. The number of points on the Poincaré section obtained from the single trajectory is 3403, and we divide the $(\rho, d\rho/dt)$ plane into 50×50 boxes to calculate the histogram. The color represents the height of the histogram, as is shown in the right of the figure.

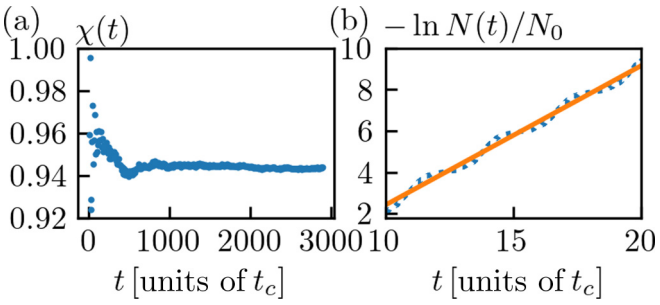

FIG. 8. Calculation of (a) the Lyapunov exponent and (b) the escape rate. (a) We calculate $\chi(t)$ by evolving the two nearby phase-space points, and we measure the deviation α_i after a time τ_i to obtain $\chi(t) = (1/\sum_i \tau_i)\sum_i \alpha_i$, from which we obtain the Lyapunov exponent from the limiting value [31,35]. (b) The dotted line represents the numerically obtained number of surviving particles as a function of time, and the solid line is the fitting curve. The slope of the curve is the escape rate.

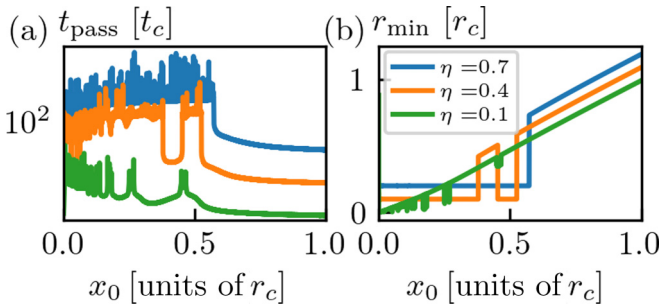

FIG. 9. (a) $t_{\rm pass}$ and (b) $r_{\rm min}$. The value of η is shown above (a). As we can see, as we increase the strength of dissipation, the fractal peak becomes broad with rapid variation and $r_{\rm min}$ is very close to zero, which means that this behavior depends strongly on the way we regularize the monopole singularity. Note that the plots are shifted upward.

the Rényi dimension D_q in three-dimensional phase space by adding 1 (which corresponds to the direction of time evolution) to the fractal dimension of the saddle on the Poincaré section, defined in Eq. (12). We obtain $D_2 = 1.51 \pm 0.02$, $D_1 = 1.52 \pm 0.02$, and $D_0 = 1.54 \pm 0.01$, so D_0 and D_1 are almost the same within the error in our model.

Finally, we calculate the Lyapunov exponent λ and the escape rate κ; see Fig. 8. We note that, since our system is a Hamiltonian system with two degrees of freedom, the energy conservation leads to a zero Lyapunov exponent, and the direction of flow corresponds to another direction with a zero Lyapunov exponent. In addition, since the symplectic structure leads to the symmetric distribution of the Lyapunov exponents around zero, the calculation of the one positive Lyapunov exponent is enough. We obtained $\lambda = 0.9437 \pm 0.0002$ and $\kappa = 0.676 \pm 0.001$. If we substitute these values into the Kantz-Grassberger formula and Young's formula, we obtain the information dimension of the saddle, $D_1 = 1 + 2(1 - \kappa/\lambda) = 1.568 \pm 0.002$, which is in accordance with the result of the calculated information dimension of the saddle D_1. In addition, from Young's formula we obtain $h_{\rm KS} = 0.268 \pm 0.001$. Also, the value of D_0 is consistent with the uncertainty exponent from the formula $D_0 = 1 + 2d_{\rm fra} = 1.52 \pm 0.02$.

Next, we discuss the stability of the chaotic behavior against the dissipative perturbation [47–49], i.e., the $-\eta\dot{\vec{r}}$ term on the right-hand side of Eq. (1); see Figs. 9 and 10. The effect of dissipation on transient chaos has been studied and is termed "doubly transient chaos" [50,51]. The two notable features in their models are as follows [50,51]: The dissipation leads to an exponential increase in the escape rate, and the fractal dimension decreases monotonically for a finer scale ($\epsilon \to 0$). The former is in accordance with our model, while the latter is in stark contrast: As for the former, as is shown in Fig. 10(b), the escape rate suddenly starts to increase around $t \sim 150$ after a long plateau region, in which $\kappa \sim 0$, in accordance with the expression of the escape rate in the presence of dissipation: $\kappa = \exp[\gamma t + \ln(\kappa_0)]$ [50]. As for the latter, we found that as we see a finer scale, the fractal dimension rapidly grows and saturates at 1; see Fig. 10. The fractal dimension may eventually decrease if we see a much finer scale [50]. Also, we note that this behavior may be due to the peculiarity of our model. Indeed, we observed a similar kind of monotonic increase in the fractal dimension in a slightly modified model in the absence of dissipation (see Appendix C), where we can attribute the increase in the fractal dimension to the infinite number of backscattering points. We note that this behavior depends strongly on the way we regularize the monopole singularity, since $r_{\rm min}$ is very close to zero around the peaks; see Fig. 9. We also found that as we increase the dissipation further, $t_{\rm pass}$ becomes smooth, and the chaos disappears.

We further verified the stability against the perturbation that breaks J_z conservation, i.e., the deformation of mass along the x direction. We calculated the fractal dimension and found that it remains finite upon deformation; see Fig. 11. From these results, we believe that the chaotic behavior we found can be observed in the experiments in which various perturbations exist.

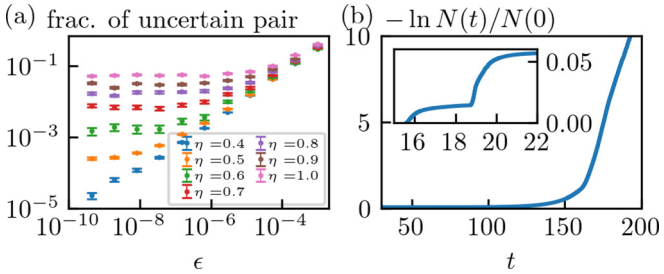

FIG. 10. (a) The fraction of an uncertain pair, and (b) the minus logarithm of the number of surviving particles. (a) As we can see, the uncertainty exponent $d_{\rm unc}$ given by the slope in (a) (the fractal dimension given by $d_{\rm fra} = 1 - d_{\rm unc}$) decreases (increases) as we see a finer scale ($\epsilon \to 0$), which is in stark contrast to doubly transient chaos. The value of η is as shown in the legend. (b) The inset shows the early time behavior, which shows linear behavior in time. After some time (around $t = 100$), the number of escaping particles suddenly increases, which indicates a monotonic increase in the escape rate.

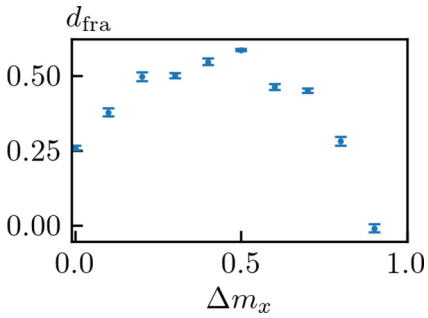

FIG. 11. The fractal dimension against the mass deformation, Δm_x. $\Delta m_x = m_x - 1$ and $\Delta m_x = 0$ is the original parameter. By increasing Δm_x, the mass along the x direction becomes large and the system becomes increasingly anisotropic.

IV. SUMMARY AND DISCUSSION

We found a fractal peak structure in t_{pass} in the problem of charged particle scattering by a magnetic monopole in the presence of a uniform electric field, and we verified that it is a consequence of the fractal nature of the saddle by calculating the quantities that characterize the saddle. Although our model has a single scatter, i.e., a monopole, the unusual nature of the scattering angle effectively leads to the scattering problem between multiple potential hills. We observed two bifurcation routes (i) by varying the electric field toward zero, where the model is solvable; and (ii) by introducing dissipation through the intermediate region where the fractal dimension increases monotonically as the scale becomes finer. We clarified the stability of the chaotic behavior against the perturbations that exist in the real experiments.

In addition, we found a divergence of t_{pass}, i.e., capture of the particle by the monopole. This is caused by the fact that the region that is accessible by the particle is bounded near the monopole, and we analytically derived the parameter region where the capturing occurs. The capturing observed here may serve as a mechanism for the bottleneck effect in which the relaxation of the excited state toward the ground state in a Born-Oppenheimer energy landscape is slowed down by the Berry curvature coming from the diabolic point.

Future work will involve a detailed discussion of symmetry-breaking deformation, i.e., mass deformation, by extending the discussion of "geometric magnetism" and "deterministic friction" [16,52] using an invariant measure on the saddle [42].

ACKNOWLEDGMENTS

The authors thank H. Ishizuka and X.-X. Zhang for useful discussions. This work was supported by JSPS KAKENHI Grant No. JP18J21329 (K.M.), JSPS KAKENHI Grants No. JP26103006, No. JP18H03676, and ImPACT Program of the Council for Science, Technology and Innovation (Cabinet office, Government of Japan), and JST CREST Grant No. JPMJCR16F1, Japan (N.N.).

APPENDIX A: DYNAMICS OF A CHARGED PARTICLE IN THE PRESENCE OF A MONOPOLE

Here, we review the analytic solution in the case of $f = 0$ [24,25,53] for completeness. The equation of motion is

$$m\ddot{\vec{r}} = q_e q_m \frac{\dot{\vec{r}} \times \vec{r}}{r^3}. \tag{A1}$$

By taking the inner product with $\dot{\vec{r}}$ and the outer product with $\vec{r}$, we obtain four conserved quantities:

$$E := \frac{m}{2}(\dot{\vec{r}})^2, \quad \vec{J} := m\vec{r} \times \dot{\vec{r}} - q_e q_m \frac{\vec{r}}{r} =: \vec{L} - q_e q_m \frac{\vec{r}}{r}. \tag{A2}$$

Among them, the independent conserved quantities are E, J_z, and $|\vec{J}|$. If we take the inner product with $\vec{r}$ and Eq. (A1), we obtain $\vec{r} \cdot \ddot{\vec{r}} = 0$, so

$$\frac{d^2 r^2}{dt^2} = 2(\dot{\vec{r}})^2 = \frac{4E}{m},$$
$$\therefore r(t) = \sqrt{(\vec{v}_0)^2 t^2 + 2(\vec{r}_0 \cdot \vec{v}_0)t + (\vec{r}_0)^2} = |\vec{v}_0 t + \vec{r}_0|, \tag{A3}$$

where $\vec{r}(0) = \vec{r}_0$ and $\dot{\vec{r}}(0) = \vec{v}_0$. We assume that $\vec{r}_0$ is not parallel to $\vec{v}_0$. Here, we take $\vec{J}$ along the z direction and we take the spherical coordinate (r, θ, ϕ). Then,

$$\frac{\vec{J} \cdot \vec{r}}{r} = -q_e q_m \Leftrightarrow \cos\theta = \frac{-q_e q_m}{J} = \frac{-q_e q_m}{\sqrt{L^2 + (q_e q_m)^2}}. \tag{A4}$$

Finally, we take the inner product of $\vec{J}$ and $\vec{L}$:

$$\vec{J} \cdot \vec{L} = J^2 - (q_e q_m)^2 \Leftrightarrow L_z = J \sin^2\theta. \tag{A5}$$

Since $L_z = mr^2 \sin^2\theta\dot{\phi}$, we obtain

$$\dot{\phi} = \frac{J}{mr^2},$$
$$\therefore \phi(t) = \frac{1}{\sin\theta}\left[\arctan\left(\frac{(\vec{v}_0)^2 t + \vec{r}_0 \cdot \vec{v}_0}{|\vec{r}_0 \times \vec{v}_0|}\right) - \arctan\left(\frac{\vec{r}_0 \cdot \vec{v}_0}{|\vec{r}_0 \times \vec{v}_0|}\right)\right]. \tag{A6}$$

Combining Eqs. (A3), (A4), and (A6), we obtained an analytical solution. From Eq. (A4), we can see that the motion of the particle is restricted on the cone oriented along $\vec{J}$ with an angle $\theta_0 = \cos^{-1}(-q_e q_m / J)$. Here we note that the motion is similar to the motion in the absence of the monopole in two aspects: the motion is restricted to the two-dimensional plane (i.e., the cone), and the trajectory on that plane is geodesic. To see the first aspect in more detail, we fix $\vec{r}_0$ and $\vec{v}_0$ and show the form of the cone in Fig. 12. Here, we set $\vec{L}(0)$ along the z axis to show the difference between the $q_e q_m < 0$ and $q_e q_m > 0$ cases (note the difference of the coordinate system from the analytic solution). We consider the process in which we start from $q_e q_m = 0$ and gradually increase to $|q_e q_m|$. That results in two modifications: The direction of the total angular momentum tilts toward the position of the particle, $\vec{r}_0$, and the surface where the trajectory of the particle lies is bent from

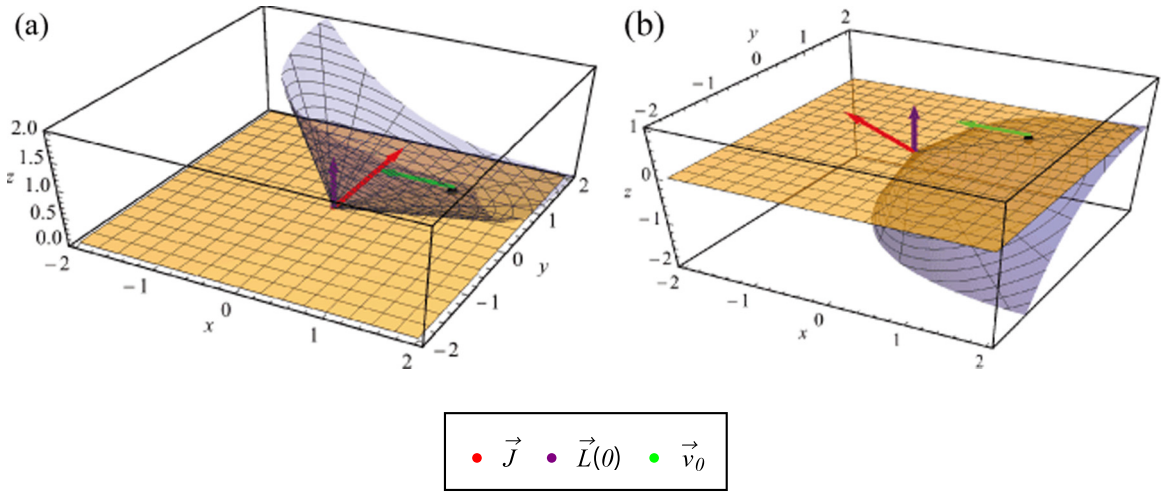

FIG. 12. The cone on which the trajectory of the particle lies (shown in blue) in the case of (a) $q_e q_m < 0$ and (b) $q_e q_m > 0$. We can see that the tilting direction of $\vec{J}$ and the bending direction of the x-y plane into the cone differ in the two cases. The black dot represents the initial position of the particle, and the red, purple, and green arrows represent $\vec{J}$, $\vec{L}(0)$, and $\vec{v}_0$, respectively. We took the z axis along the $\vec{L}(0)$ direction, which coincides with $\vec{J}$ in the case of $q_e q_m = 0$, and the orange plane represents the x-y plane.

the x-y plane into the cone. We note that, since the x-y plane is tangential to the cone at $\vec{r}_0$ and the initial velocity is along the x-y plane, the particle will not get out of the cone [45]. Since the trajectory of the particle at $q_e q_m = 0$ is the geodesic on the x-y plane, we expect the motion of the particle on the cone to also be the geodesic. To verify that this is correct, we define χ as the angle between $\vec{r}_0$ and $\vec{v}_0$. Then,

$$\frac{\vec{r}_0 \cdot \vec{v}_0}{|\vec{r}_0 \times \vec{v}_0|} = \cot\chi = \tan\left(\frac{\pi}{2} - \chi\right), \tag{A7}$$

so from Eq. (A6),

$$\begin{aligned}\frac{(\vec{v}_0)^2 t + \vec{r}_0 \cdot \vec{v}_0}{|\vec{r}_0 \times \vec{v}_0|} &= \tan\left(\sin\theta\phi(t) + \frac{\pi}{2} - \chi\right) \\ &= -\cot[\sin\theta\phi(t) - \chi],\end{aligned}$$

therefore,

$$\begin{aligned}&\frac{(\vec{v}_0)^2 r(t)^2 + (\vec{r}_0 \cdot \vec{v}_0)^2 - (\vec{v}_0)^2(\vec{r}_0)^2}{|\vec{r}_0 \times \vec{v}_0|^2} \\ &= \cot^2[\sin\theta\phi(t) - \chi] \quad [\because \text{Eq. (A3)}] \\ &\Leftrightarrow \frac{(\vec{v}_0)^2 r(t)^2}{|\vec{r}_0 \times \vec{v}_0|^2} = \cot^2[\sin\theta\phi(t) - \chi] + 1 \\ &\therefore\ r(t)\sin[\chi - \sin\theta\phi(t)] = r_0 \sin\chi. \end{aligned} \tag{A8}$$

To understand this equation, we expand the cone to obtain its development, and we consider the two-dimensional motion on that. Then, the quantity $\sin\theta\phi(t)$ represents the angle between $\vec{r}_0$ and $\vec{r}(t)$ in the development of the cone. Since χ represents the angle between $\vec{r}_0$ and $\vec{v}_0$, the above equation can be rewritten as

$$\vec{v}_0 \cdot \vec{r}(t) = \vec{v}_0 \cdot \vec{r}_0 \quad \text{on the development of the cone.} \tag{A9}$$

This means that the motion of the particle is a straight line on the development. In other words, the trajectory is geodesic for the flat metric induced by (locally) identifying the development of the cone with two-dimensional Euclidean space. In this sense, the trajectory is still "straight," although in three-dimensional space it looks complicated.

One important feature that is relevant for the main text is Eq. (A3). It means that the monopole does not attract the particle to cause the delay in the passing of the particle near the origin.

APPENDIX B: HAMILTON-JACOBI EQUATION

Here we solve the $f = 0$ case with the Hamilton-Jacobi method, which may serve as a good starting point for further analysis with perturbation theory. The Hamiltonian for Eq. (3) obtained by the Legendre transformation is the following:

$$H = \frac{p_r^2}{2m} + \frac{1}{2mr^2}\left[p_\theta^2 + \frac{1}{\sin^2\theta}(p_\phi + q_m q_e \cos\theta)^2\right]. \tag{B1}$$

The Hamilton-Jacobi equation for this Hamiltonian is

$$\begin{aligned}&\frac{\partial S}{\partial t} + H\left(q_i, \frac{\partial S}{\partial q_i}\right) = 0 \\ &\Leftrightarrow \frac{\partial S}{\partial t} + \frac{1}{2m}\left(\frac{\partial S}{\partial r}\right)^2 \\ &\quad + \frac{1}{2mr^2}\left[\left(\frac{\partial S}{\partial \theta}\right)^2 + \frac{1}{\sin^2\theta}\left(\frac{\partial S}{\partial \phi} + q_m q_e \cos\theta\right)^2\right] = 0.\end{aligned} \tag{B2}$$

Since the energy is conserved, ϕ is the cyclic coordinate, and r and θ are separable, and we set $S = -\epsilon t + W_r(r) + W_\theta(\theta) + \alpha_\phi \phi$ to obtain

$$\left(\frac{\partial W_\theta}{\partial \theta}\right)^2 + \frac{1}{\sin^2\theta}(\alpha_\phi + q_m q_e \cos\theta)^2 = \alpha_\theta^2 - (q_e q_m)^2, \tag{B3}$$

$$\left(\frac{\partial W_r}{\partial r}\right)^2 + \frac{\alpha_\theta^2 - (q_e q_m)^2}{r^2} = 2m\epsilon, \tag{B4}$$

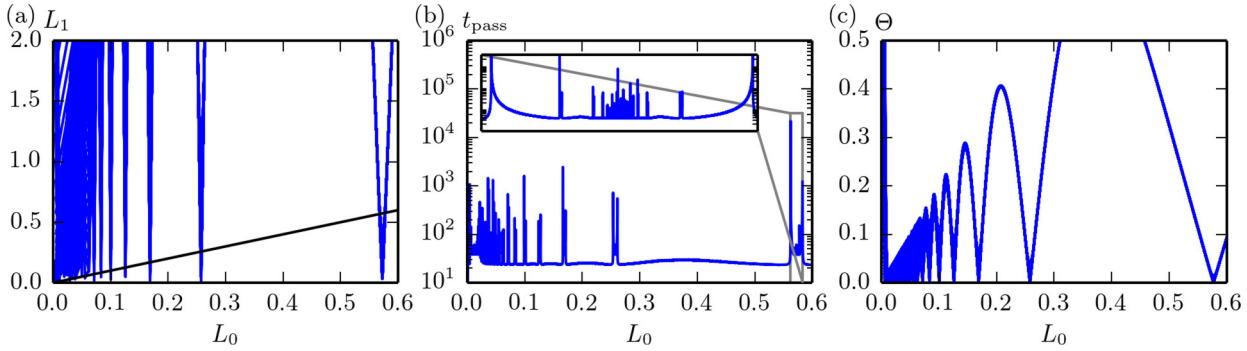

FIG. 13. L_1, $t_{\rm pass}$, and Θ as a function of L_0 at $A = B = 10$. As we can see, the peak of $t_{\rm pass}$ is near the region where $L_0 = L_1$ holds.

where α_θ and α_ϕ correspond to $|\vec{J}|$ and J_z, respectively. At this point, ϵ, α_θ, and α_ϕ are constants of motion. These equations can be transformed to

$$W_\theta = -\int d\theta \sqrt{\alpha_\theta^2 - (q_e q_m)^2 - \frac{1}{\sin^2\theta}(q_e q_m \cos\theta + \alpha_\phi)^2}, \tag{B5}$$

$$W_r = \int dr \sqrt{2m\epsilon - \frac{\alpha_\theta^2 - (q_e q_m)^2}{r^2}}, \tag{B6}$$

where we chose the minus sign for W_θ just for convenience. Then, we calculate $\beta_i(q_i, \alpha_i) := \frac{\partial S}{\partial \alpha_i}$, which are canonically conjugate to α_i and are the remaining constants of motion. After a somewhat long but straightforward calculation, we obtain

$$\beta_\phi := \frac{\partial S}{\partial \alpha_\phi} = \phi - \frac{\pi}{2} + \arctan\left[\frac{\cos A \sin i - \cos i \sin A \sin\psi}{\cos\psi \sin A}\right], \tag{B7}$$

$$\beta_\theta := \frac{\partial S}{\partial \alpha_\theta} = \frac{1}{\sin A}\left(\frac{\pi}{2} - \arctan\left[\sqrt{\frac{2m\epsilon r^2}{\alpha_\theta^2 \sin^2 A} - 1}\right]\right) + \psi, \tag{B8}$$

$$\beta_0 := \frac{\partial S}{\partial \epsilon} = -t + \sqrt{\frac{m}{2\epsilon}}\sqrt{r^2 - \frac{\alpha_\theta^2 \sin^2 A}{2m\epsilon}}, \tag{B9}$$

where

$$\cos\theta = \sin A \sin i \sin\psi + \cos A \cos i, \tag{B10}$$

$$\cos A := \frac{-q_e q_m}{\alpha_\theta}, \tag{B11}$$

$$\cos i := \frac{\alpha_\phi}{\alpha_\theta}. \tag{B12}$$

By solving Eqs. (B7), (B8), and (B9) for (r, ψ, ϕ), noting that we are free to add $\Delta S(\alpha_i)$ to S to shift each β_i by any function of α_i, we obtain

$$r(t) = \sqrt{\frac{2\epsilon}{m}(t+\beta_0)^2 + \frac{\alpha_\theta^2 \sin^2 A}{2m\epsilon}}, \tag{B13}$$

$$\psi(t) = \beta_\theta + \frac{1}{\sin A}\arctan\left[\frac{2\epsilon}{\alpha_\theta \sin A}(t+\beta_0)\right], \tag{B14}$$

$$\phi(t) = \beta_\phi - \arctan\left[\frac{\cos A \sin i - \cos i \sin A \sin\psi(t)}{\cos\psi(t)\sin A}\right]. \tag{B15}$$

Note that if we substitute

$$\beta_0 = \frac{\vec{v}_0 \cdot \vec{r}_0}{(v_0)^2}, \tag{B16}$$

$$\beta_\theta = -\frac{1}{\sin A}\arctan\left[\frac{2\epsilon\beta_0}{\alpha_\theta \sin A}\right] \tag{B17}$$

into Eqs. (B13) and (B14), we reproduce Eqs. (A3) and (A6).

APPENDIX C: ON THE PEAK STRUCTURE OF $t_{\rm pass}$

To understand the peak structure of $t_{\rm pass}$, we consider the following toy model, which can be smoothly deformed to our model: We put the potential barrier at the $z = -A < 0$

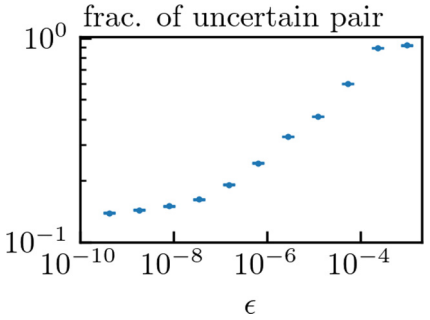

FIG. 14. The fraction of an uncertain pair. As we can see, the uncertainty exponent $d_{\rm unc}$ given by the slope (the fractal dimension given by $d_{\rm fra} = 1 - d_{\rm unc}$) decreases (increases) as we see a finer scale ($\epsilon \to 0$). The calculation was done for the peak around $L_0 = 0.6$ with $A = B = 10$; see Fig. 13(b).

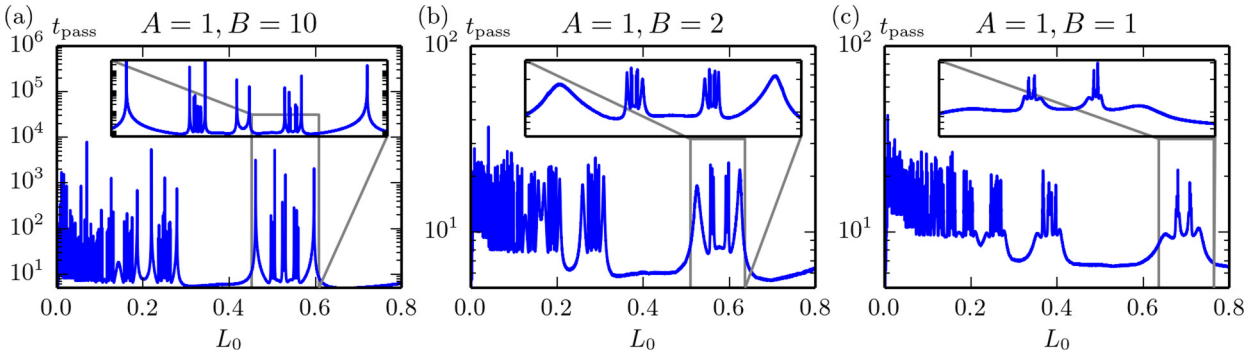

FIG. 15. L_1, $t_{\rm pass}$, and Θ as a function of L_0. As we can see, the peak of $t_{\rm pass}$ is near the region where $L_0 = L_1$ holds.

plane, and we consider the motion of the particle bouncing back and forth between this potential barrier and the magnetic monopole at the origin. We start from the limit where the barrier is steplike and far from the origin, and we smoothly vary the position and thickness of the barrier to reach the limit where the potential can be regarded as the one imitating the uniform electric field.

More concretely, we consider a potential of the form $U(z) = 1 - \tanh[(z + A)/B]$, where A represents the position of the wall and B represents the width of the slope of the potential. We set the initial condition as $\vec{v}_0 = \vec{0}$ and $(x_0, y_0, z_0) = (0, 0, -A)$, and we calculate $L = |\vec{r} \times \vec{v}|$ and v_z at the first two intersections with the Poincaré section at $z = -A + 1$ with $v_z > 0$. We note that, because of J_z and E conservation, the effective phase-space degree of freedom is 3, so the Poincaré map is defined as $(L_n, v_{z,n}) \to (L_{n+1}, v_{z,n+1})$. We show L_1, $t_{\rm pass}$, and $\Theta := \arccos(\vec{v}_0 \cdot \vec{v}_1)$ as a function of L_0 in Fig. 13. As we can see, a complicated peak structure is observed near the point where $L_0 = L_1$ holds. We note that near these regions, $\Theta \sim 0$, so we speculate that the Poincaré map can be approximated as $(L_n) \to (L_{n+1})$ at least for this initial regime. By considering the web diagram in Fig. 13(a), we can understand the complicated peak structure of Fig. 13(b): The particles that start from the points sandwiched between the crossing points of blue and black lines go to the smaller L region, and among them some particles again get to the region sandwiched between the crossing points and mapped to the smaller L region, and so on. Therefore, we conclude that the complicated peak structure of $t_{\rm pass}$ [Fig. 13(b)] and the monotonic increase of the fractal dimension as a function of scale (Fig. 14) are caused by the infinite number of backscattering points, around which L is mapped to a smaller value.

As we deform A and B to reach the model that is similar to our model with a uniform electric field, these peak structures evolve into a fractal peak; see Fig. 15. So, from the argument above, we speculate that the multiple backscattering points play the role of the potential hills in the usual chaotic scattering [30,31], thereby producing the infinite number of symbols sequence by labeling each backscattering point by an integer.

APPENDIX D: THE CHANGE OF $U_{\rm eff}$ FROM THE VARIATION OF f

We consider a one-parameter family that connects the equation of motion for Eq. (5), where $U(\rho, z) = -fz$, to the one where $U(\rho, z) = 0$, which is the solvable limit. We define $\tilde{r}_c = |q_m q_e|/\sqrt{mE}$ and $\tilde{t}_c = |q_m q_e|/E$. Then the equation of motion can be rewritten as

$$\frac{d^2\tilde{Z}}{d\tilde{\tau}^2} = -\frac{\partial \tilde{U}_{\rm eff}}{\partial \tilde{Z}}, \quad \frac{d^2\tilde{P}}{d\tilde{\tau}^2} = -\frac{\partial \tilde{U}_{\rm eff}}{\partial \tilde{P}}, \quad \tilde{U}_{\rm eff} := -F\tilde{Z} + \frac{1}{2}\left(\frac{J_z}{q_m q_e} + \frac{\tilde{Z}}{\sqrt{\tilde{Z}^2 + \tilde{P}^2}}\right)^2, \tag{D1}$$

where $\tilde{Z} = z/\tilde{r}_c$, $\tilde{P} = \rho/\tilde{r}_c$, $\tilde{\tau} = t/\tilde{t}_c$, and $F = f\tilde{r}_c/E$. The change of $U_{\rm eff}$ as a function of F is shown in Fig. 16.

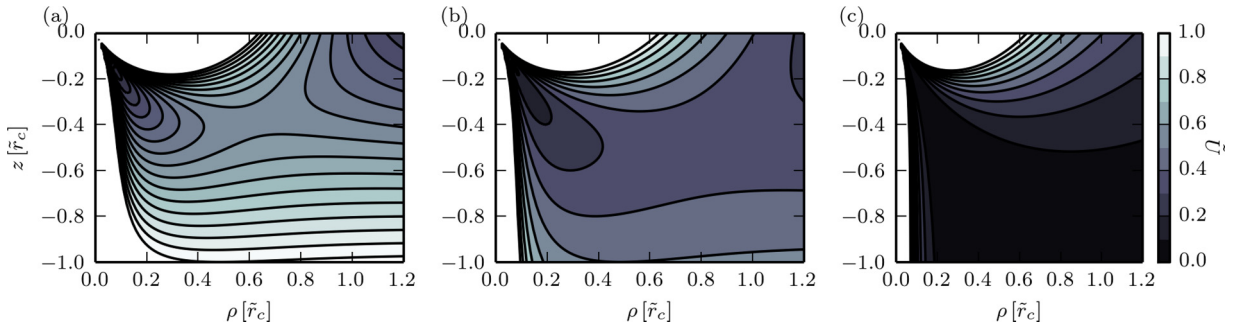

FIG. 16. The change of $U_{\rm eff}$ by varying the dimensionless force parameter, F. Here we set $J_z/(q_m q_e) = 0.9$, and (a) $F = 1$, (b) $F = 0.5$, and (c) $F = 0$.

[1] P. A. M. Dirac, Proc. R. Soc. London, Ser. A **133**, 60 (1931).
[2] G. 't Hooft, Nucl. Phys. B **79**, 276 (1974).
[3] A. M. Polyakov, Pis'ma Zh. Eksp. Teor. Fiz. **20**, 430 (1974) [JETP Lett. **20**, 194 (1974)].
[4] C. Castelnovo, R. Moessner, and S. L. Sondhi, Nature (London) **451**, 42 (2008).
[5] M. V. Berry, Proc. R. Soc. London, Ser. A **392**, 45 (1984).
[6] J. Dalibard, F. Gerbier, G. Juzeliūnas, and P. Öhberg, Rev. Mod. Phys. **83**, 1523 (2011).
[7] N. Goldman, G. Juzeliūnas, P. Öhberg, and I. B. Spielman, Rep. Prog. Phys. **77**, 126401 (2014).
[8] P. Zhang, Y. Li, and C. P. Sun, Eur. Phys. J. D **36**, 229 (2005).
[9] J. Ruseckas, G. Juzeliūnas, P. Öhberg, and M. Fleischhauer, Phys. Rev. Lett. **95**, 010404 (2005).
[10] M. W. Ray, E. Ruokokoski, S. Kandel, M. Möttönen, and D. Hall, Nature (London) **505**, 657 (2014).
[11] S. Murakami, New J. Phys. **9**, 356 (2007).
[12] X. Wan, A. M. Turner, A. Vishwanath, and S. Y. Savrasov, Phys. Rev. B **83**, 205101 (2011).
[13] P. Hosur and X. Qi, C. R. Phys. **14**, 857 (2013).
[14] N. P. Armitage, E. J. Mele, and A. Vishwanath, Rev. Mod. Phys. **90**, 015001 (2018).
[15] M. Berry and J. Robbins, Proc. R. Soc. London, Ser. A **442**, 641 (1993).
[16] M. Berry and J. Robbins, Proc. R. Soc. London, Ser. A **442**, 659 (1993).
[17] G. Sundaram and Q. Niu, Phys. Rev. B **59**, 14915 (1999).
[18] D. Xiao, M.-C. Chang, and Q. Niu, Rev. Mod. Phys. **82**, 1959 (2010).
[19] P. Goddard and D. I. Olive, Rep. Prog. Phys. **41**, 1357 (1978).
[20] J. Preskill, Annu. Rev. Nucl. Part. Sci. **34**, 461 (1984).
[21] D. Tong, arXiv:hep-th/0509216.
[22] Y. M. Shnir, *Magnetic Monopoles*, Text and Monographs in Physics (Springer, Berlin, 2005).
[23] K. McDonald, Birkeland, Darboux and Poincaré: Motion of an Electric Charge in the Field of a Magnetic Pole, http://www.physics.princeton.edu/~mcdonald/examples/birkeland.pdf.
[24] G. Darboux, Bull. Sci. Math. Astron. **2**, 433 (1878).
[25] H. Poincaré, C. R. Acad. Sci. **123**, 530 (1896).
[26] C. Jung, J. Phys. A **19**, 1345 (1986).
[27] B. Eckhardt, J. Phys. A **20**, 5971 (1987).
[28] B. Eckhardt, Physica D **33**, 89 (1988).
[29] C. Jung and S. Pott, J. Phys. A **22**, 2925 (1989).
[30] P. Gaspard and S. A. Rice, J. Chem. Phys. **90**, 2225 (1989).
[31] S. Bleher, C. Grebogi, and E. Ott, Physica D **46**, 87 (1990).
[32] B. Simon, Phys. Rev. Lett. **51**, 2167 (1983).
[33] H. Goldstein, C. Poole, and J. Safko, *Classical Mechanics*, 3rd ed. (Pearson, Hoboken, 2002).
[34] C. K. Birdsall and A. B. Langdon, *Plasma Physics Via Computer Simulation* (McGraw-Hill, New York, 1985).
[35] E. Ott, *Chaos in Dynamical Systems* (Cambridge University Press, Cambridge, 2002).
[36] Y.-C. Lai and T. Tél, *Transient Chaos* (Springer, New York, 2011).
[37] D. G. Boulware, L. S. Brown, R. N. Cahn, S. Ellis, and C. Lee, Phys. Rev. D **14**, 2708 (1976).
[38] J. Schwinger, K. A. Milton, W.-Y. Tsai, L. L. DeRaad, and D. C. Clark, Ann. Phys. **101**, 451 (1976).
[39] S. Smale, Bull. Am. Math. Soc. **73**, 747 (1967).
[40] Q. Chen, M. Ding, and E. Ott, Phys. Lett. A **145**, 93 (1990).
[41] H. Kantz and P. Grassberger, Physica D **17**, 75 (1985).
[42] P. Gaspard, *Chaos, Scattering and Statistical Mechanics* (Cambridge University Press, Cambridge, 2005), Vol. 9.
[43] L.-S. Young, Ergodic Theory Dyn. Syst. **2**, 109 (1982).
[44] Y.-T. Lau, J. M. Finn, and E. Ott, Phys. Rev. Lett. **66**, 978 (1991).
[45] In other words, once the direction of $\vec{J}$ is fixed from Eq. (A2), then the opening angle is automatically determined from the requirement that the cone should be tangential to the plane subtended by the vectors $\vec{r}_0$ and $\vec{v}_0$.
[46] H. E. Nusse and J. A. Yorke, Physica D **36**, 137 (1989).
[47] A. E. Motter and Y.-C. Lai, Phys. Rev. E **65**, 015205 (2001).
[48] J. M. Seoane, J. Aguirre, M. A. Sanjuán, and Y.-C. Lai, Chaos **16**, 023101 (2006).
[49] J. M. Seoane, M. A. F. Sanjuán, and Y.-C. Lai, Phys. Rev. E **76**, 016208 (2007).
[50] A. E. Motter, M. Gruiz, G. Károlyi, and T. Tél, Phys. Rev. Lett. **111**, 194101 (2013).
[51] X. Chen, T. Nishikawa, and A. E. Motter, Phys. Rev. X **7**, 021040 (2017).
[52] M. V. Berry and E. C. Sinclair, J. Phys. A **30**, 2853 (1997).
[53] K. Nakamura, Bull. Arts Sci., Meiji Univ. **181**, 1 (1985).